

1 **Impact of momentum perturbation on convective**  
2 **boundary layer turbulence**

3 Mukesh Kumar<sup>1,2,\*</sup>, Alex Jonko<sup>2</sup>, William Lassman<sup>3</sup>, Jeffrey D. Mirocha<sup>3</sup>,  
4 Branko Kosović<sup>4</sup>, and Tirtha Banerjee<sup>1</sup>

5 <sup>1</sup>Department of Civil and Environmental Engineering, University of California,  
6 Irvine, CA, USA

7 <sup>2</sup>Los Alamos National Laboratory, NM, USA

8 <sup>3</sup>Lawrence Livermore National Laboratory, CA, USA

9 <sup>4</sup>National Center for Atmospheric Research, CO, USA

10 \*Correspondence to: Mukesh Kumar, mukeshk@uci.edu

11 January, 2022

12 **Abstract**

13 Mesoscale-to-microscale coupling is an important tool to conduct turbulence-resolving mul-  
14 tiscala simulations of realistic atmospheric flows, which are crucial for applications ranging  
15 from wind energy to wildfire spread studies. Different techniques are used to facilitate the  
16 development of realistic turbulence in the large-eddy simulation (LES) domain while min-  
17 imizing computational cost. Here, we explore the impact of a simple and computationally  
18 efficient Stochastic Cell Perturbation method using momentum perturbation (SCPM-M) to  
19 accelerate turbulence generation in boundary-coupled LES simulations using the Weather  
20 Research and Forecasting (WRF) model. We simulate a convective boundary layer (CBL) to  
21 characterize the production and dissipation of turbulent kinetic energy (TKE) and the vari-  
22 ation of TKE budget terms. Furthermore, we evaluate the impact of applying momentum  
23 perturbations of three magnitudes below, up to, and above the CBL on the TKE bud-  
24 get terms. Momentum perturbations greatly reduce the fetch associated with turbulence  
25 generation. When applied to half the vertical extent of the boundary layer, momentum

26 perturbations produce an adequate amount of turbulence. However, when applied above  
27 the CBL, additional structures are generated at the top of the CBL, near the inversion  
28 layer. The magnitudes of the TKE budgets produced by SCPM-M when applied at varying  
29 heights and with different perturbation amplitudes are always higher near the surface and  
30 inversion layer than those produced by No-SCPM, as are their contributions to the TKE.  
31 This study provides a better understanding of how SCPM-M reduces computational costs  
32 and how different budget terms contribute to TKE in a boundary-coupled LES simulation.

33 **Keywords:** Convective Boundary Layer, Large Eddy Simulation, Nesting, Turbulence genera-  
34 tion, Turbulence Kinetic Energy Budget

### 35 **Key Points**

- 36 **1.** The fetch is reduced after applying momentum perturbation and the reduction is directly  
37 proportional to the amplitude of the perturbations.
- 38 **2.** Applying momentum perturbation up to half the boundary layer height produces an adequate  
39 amount of turbulence without additional entrainment.
- 40 **3.** Momentum perturbations result in TKE budget terms of higher magnitude than simulations  
41 without perturbations.

### 42 **Plain Language Summary**

43 Grid nesting is a technique in atmospheric modeling where smaller model domains with finer  
44 resolutions are embedded in larger domains with coarser resolutions, allowing us to simulate  
45 processes for which a range of resolutions is important. When nesting a micro-scale domain, which  
46 resolves atmospheric turbulence, within a mesoscale domain, where turbulence is parameterized  
47 instead, the micro-scale domain needs to generate turbulence. This can take a long distance,  
48 reducing the area within the micro-scale domain where turbulence is fully developed. Turbulence  
49 generation methods can speed up this process, leading to more efficient multi-scale simulations.  
50 Here, we take a close look at one such turbulence generation method, which applies random  
51 perturbations to the momentum field along the boundaries of the micro-scale domain. We test  
52 several different configurations of momentum perturbations and evaluate their impacts on the  
53 turbulent kinetic energy budget within the micro-scale domain. Our results can be used as  
54 guidance on how to apply momentum perturbations most efficiently in grid-nested simulations.

## 55 1 Introduction

56 Grid nesting for mesoscale-to-large-eddy simulation (LES) is a useful technique for a variety  
57 of atmospheric model applications, from wind energy to wildfire spread investigations (Haupt  
58 et al., 2020, 2019a,b; Mazzaro et al., 2019; Mirocha et al., 2014; Ching et al., 2014; Connolly  
59 et al., 2021; Rai et al., 2017b). In LES, realistic atmospheric turbulence emerges as a result  
60 of wind shear and buoyant forcing. However, realistic turbulence can require a long distance  
61 to develop. Turbulence generation methods can accelerate the generation of turbulence in the  
62 LES domain, effectively reducing the distance it takes for turbulent motions to develop, known  
63 as fetch. A common approach is to use a periodic domain where wind through the outflow  
64 boundary is recycled through the inflow boundary, retaining memory of the flow characteristics.  
65 However, periodic simulations are limited in their ability to represent heterogeneous surfaces or  
66 flow around obstacles. For these applications, a boundary-coupled simulation with an inflow and  
67 outflow is required (Liu et al., 2011; Talbot et al., 2012; Zhou and Chow, 2013; Mirocha et al.,  
68 2014; Muñoz-Esparza et al., 2015, 2017; Mazzaro et al., 2017, 2019; Rai et al., 2017a; Jähn et al.,  
69 2016; Connolly et al., 2021). In boundary-coupled simulations using inflow data that does not  
70 contain resolved turbulence at the time and space scales of the LES discretization (e.g. from  
71 a mesoscale simulation), the development of resolved-scale turbulence generally requires a long  
72 fetch. Therefore, a large LES domain is needed (Mazzaro et al., 2017, 2019; Mirocha et al.,  
73 2014; Muñoz-Esparza et al., 2014b,a; Zajaczkowski et al., 2011; Tabor and Baba-Ahmadi, 2010)  
74 to capture the development of turbulence at fine scales, increasing computational cost (Mirocha  
75 et al., 2010, 2014; Connolly et al., 2021; Muñoz-Esparza et al., 2014b; Mazzaro et al., 2017, 2019;  
76 Giani et al., 2022). The concept of "time" is used to clarify the time that a parcel of air entering  
77 the inflow boundary experiences. One way to reduce the fetch is to run a precursor LES using  
78 periodic lateral boundary conditions with the same time and space discretization as the target  
79 LES, and use the solution as inflow (Muñoz-Esparza et al., 2016; Deardorff, 1972, 1980; Smith and  
80 Skillingstad, 2009; Sauer et al., 2016; Moeng and Wyngaard, 1984; Moeng and Sullivan, 1994).  
81 However, the precursor simulation can require significant additional computational overhead,  
82 while also requiring forcing and surface conditions amenable to periodicity.

83 To overcome these challenges, a class of methods exists to initialize inflow boundary conditions  
84 with turbulence. For example, synthetic turbulence methods (Le et al., 1997; Pamiès et al., 2009)  
85 use digital filtering techniques of flow to infer Reynolds Stresses (Di Mare et al., 2006; Klein et al.,  
86 2003; Xie and Castro, 2008). These techniques require some information about the turbulence,

87 either from observations or a periodic simulation. These methods also require relatively long  
88 fetches for the generation of turbulence. Another technique is the forcing method (Spille-Kohoff  
89 and Kaltenbach, 2001; Zajaczkowski et al., 2011; Keat et al., 2004), which uses wall-normal  
90 forces to move the flow into the domain inlet and generate the necessary Reynolds shear stress.  
91 However, it also needs a *priori* information about the targeted level of turbulence. Additional  
92 simulations are needed for generating an adequate amount of turbulence from this method in  
93 order to get a value that is closer to the observation.

94 As a compromise to using a turbulent inflow condition, another approach is to seed the inflow  
95 characteristics with added perturbations and allow the flow to develop realistic turbulence over  
96 a reduced fetch. One such method, the cell perturbation Method (CPM) (Muñoz-Esparza et al.,  
97 2014b, 2015; Muñoz-Esparza and Kosović, 2018), is a turbulence generation technique that em-  
98 ploys random perturbations to potential temperature to induce small-scale motions near nested  
99 domain inflow boundaries. Mazzaro et al. (2019) modified the CPM approach by applying force  
100 perturbations to the momentum in the horizontal and vertical directions rather than perturbing  
101 the potential temperature fields. Mirocha et al. (2014) applied tendencies with sinusoidal am-  
102 plitudes to temperature and velocity fields near inflow boundaries. This perturbation method  
103 produced promising results with the target turbulence level by triggering turbulent motions near  
104 the nested domain inflow boundaries. Muñoz-Esparza et al. (2014b, 2015), and Muñoz-Esparza  
105 and Kosović (2018) advanced this method by adding random forces instead of using sinusoidal  
106 perturbations, and also introduced perturbation cells. Perturbation cells are a span of contigu-  
107 ous model grid points located adjacent to the LES inflow boundaries that are perturbed with  
108 the same random value. A configuration of three cells consisting of eight grid points per cell in  
109 each of the horizontal directions is found to be optimal (Muñoz-Esparza et al., 2014b). In addi-  
110 tion, Muñoz-Esparza and Kosović (2018) optimized the CPM for different stability conditions.  
111 Thermal perturbations are chosen to encourage the most rapid formation of realistic correlations  
112 associated with buoyancy forces generated by the patches of resolved temperature variability.  
113 Although this optimization reduces the fetch size considerably relative to simulations using no  
114 perturbations, a nontrivial fetch still remains.

115 To further reduce the fetch required for turbulence generation, Mazzaro et al. (2019) applied  
116 tendencies directly to the momentum components, rather than potential temperature. This  
117 study showed that simulation perturbations that were applied to the vertical momentum term  
118 produced the shortest fetches overall, thereby further reducing fetch requirements and associ-  
119 ated computational costs. However, the consequence of introducing momentum perturbations

120 at the domain boundary on the fate and transport of turbulence in the domain is not yet well  
121 understood (Mazzaro et al., 2019). Quantifying the TKE budget in the Weather Research and  
122 Forecasting (WRF) LES domain can shed light on this question. In this study, we examine how  
123 momentum perturbations shift the balance between the terms of the TKE budget in the convec-  
124 tive boundary layer (CBL). We apply random (stochastically selected from within an amplitude  
125 range of  $1,000 \text{ kgs}^{-4}$  to  $10,000 \text{ kgs}^{-4}$ ) forces in both vertical and horizontal directions and vary  
126 the vertical extent of the perturbations from 307 m (halfway between the surface and boundary  
127 layer and 1,608 m (top of the domain). TKE budget terms, including buoyant production, shear  
128 production, turbulent transport, and pressure correlation are then compared between simulations  
129 including these different perturbation configurations, periodic simulations, and simulations not  
130 including perturbations.

131 The goals of this study are as follows: (1) to explore the impact of a simple and compu-  
132 tationally efficient Stochastic Cell Perturbation method (SCPM) to accelerate the generation  
133 of turbulence; (2) to understand how momentum perturbations shift the balance between the  
134 terms of the TKE budget; (3) to evaluate the role of momentum perturbation amplitudes on the  
135 TKE budget; and (4) to examine the effect of height in a convective boundary layer at which  
136 momentum perturbations are applied. We use the WRF LES model to simulate the convective  
137 boundary layer. Our results will advance the understanding of optimal strategies for performing  
138 coupled mesoscale-microscale simulations of atmospheric boundary layer processes.

139 This study is organized into three main sections. The methods and experimental set-up  
140 that are used to perform the SCPM using momentum perturbations (SCPM-M) are presented  
141 in section 2. Section 3 describes the results and discussion of our analysis. Conclusions are  
142 presented in section 4.

## 143 **2 Methods**

### 144 **2.1 Model Configuration**

145 In this study, we examine the impacts of applying SCPM-M in a convective (unstable) atmo-  
146 spheric boundary layer on the TKE budget. We use the WRF model version 4.1.3 (Skamarock  
147 et al., 2019) to conduct idealized LES simulations of a convective boundary layer based on mea-  
148 surements at the Scaled Wind Farm Technology (SWiFT) facility. The SWiFT site is located in  
149 west Texas’s southern Great Plains and features nearly uniform terrain elevation covered with

150 grass and small bushes. The site contains a 200 m meteorological tower that provided fast-  
151 response velocity and temperature data at 10 heights between 0.9 and 200 m from which mean  
152 and turbulence quantities could be computed.

153 To conduct our analysis of the SCPM-M method, we utilized an idealized nested LES setup  
154 with forcing that approximated the observed flow conditions occurring during a two-hour pe-  
155 riod during the afternoon of November 8<sup>th</sup>, 2013, 18 Z - 20 Z. We used a two-domain nested  
156 configuration for which periodic lateral boundary conditions were applied on the outer domain,  
157 and the inner domain received lateral boundary data from the bounding domain solution. The  
158 goal of the setup was to closely approximate the observed mean wind speed and atmospheric  
159 stability observed during the case study period on the outer domain. We could then examine the  
160 representation of turbulence on the inner domain and also assess the efficacy of the perturbations  
161 to accelerate the formation and fidelity of the turbulence, relative to observed values.

162 Since the terrain was negligible, we approximated the surface as flat, with a uniform roughness  
163 length of 0.03 m. A very close agreement between the simulated and observed wind speeds across  
164 the depth of the tower was then produced by using a constant geostrophic forcing of  $(u_g, v_g) =$   
165  $(15.331, -9.431) \text{ ms}^{-1}$ , and a surface sensible heat flux of  $175 \text{ W/m}^2$ , which approximated the  
166 mean observed values from the lowest sensor height on the tower (0.9 m). These values ensured  
167 that the simulated wind direction aligned with the x-direction, allowing for the use of a nested  
168 domain elongated in the mean flow direction to facilitate the examination of the developing  
169 turbulence.

170 Simulations were initiated using a constant potential temperature between the surface and  
171 250 m, with a capping inversion of 288 K/m applied up to the model top of approximately 1600  
172 m. The simulations were run for 6 hours with the first four used for spin-up, and the latter two  
173 used for examination. The WRF domains used horizontal grid resolutions of 240 m and 12 m  
174 where the inner LES domain is one-way nested within an idealized mesoscale domain. Here, the  
175 effective WRF grid resolution (1440 m = 6x240 m) is larger than the CBL height (600 m) and  
176 therefore the inflow conditions would not contain any resolved turbulence. The mesoscale domain  
177 (d01) has a horizontal extent of 115 km by 115 km, with 480 grid cells in both  $X$  and  $Y$  directions,  
178 while the LES domain (d02) has 961 grid cells in  $X$  direction and 481 grids in  $Y$  for a domain  
179 size of 11.5 km by 5.7 km. We use 88 vertical eta levels with the top level at 1,608 m (ztop).  
180 The minimum and maximum vertical grid spacing are 2.0032 m and 1606.5122 m respectively.  
181 An input sounding is used from the SWiFT facility with a capping inversion at approximately  
182 600 m. The time step for integration is 0.5 seconds for the mesoscale domain and the outputs

183 for the LES domain are stored every minute. We use a parent time step ratio of 50 and a  
184 resulting LES time step of 0.01 seconds. The general information on the model configuration  
185 is summarized in Table 2. Overall we perform nine WRF-LES simulations. The perturbation  
186 amplitudes chosen here are based on the work of Mazzaro et al. (2019), from which we selected  
187 a combination of all perturbation amplitudes, including the maximum amplitude, where each of  
188 these amplitudes is chosen at random from a uniform distribution (Mazzaro et al., 2019) that  
189 is defined by the largest perturbation value ( $Fxy = 5,000 \text{ kgs}^{-4}$  &  $Fz = 10,000 \text{ kgs}^{-4}$ ). The  
190 conversion of force perturbation amplitude into equivalent acceleration is nonlinear because the  
191 WRF transport equations are dependent on the mass in the system (Mazzaro et al., 2019). The  
192 acceleration that results from an individual force disturbance is inversely proportional to the  
193 pressure that the atmospheric column is exerting above the affected region. Instead of simply  
194 changing the individual velocity components, we take a novel technique (SCPM-M) and change  
195 the scalar tendency of the components. The model's equations of motion are able to calculate  
196 variations in velocity because of the fluctuations we introduce in such a manner (Mazzaro et al.,  
197 2019). Seven WRF-LES simulations are performed using various permutations of perturbation  
198 height and magnitude. In addition, we also perform one simulation with no inflow perturbations  
199 (referred to as No-SCPM) and another simulation with periodic boundary conditions (referred  
200 to as periodic) for context. By using periodic boundary conditions, it is implicitly assumed that  
201 both the atmospheric fields and the underlying land usage are encountered periodically during  
202 the simulation (Mirocha et al., 2014; Zhong et al., 2021). These simulations are summarized in  
203 Table 1 and described in more detail in section 2.2.

204 We use the YSU (Hong et al., 2006) PBL scheme for the mesoscale domain. We do not use  
205 cloud microphysics, land surface, cumulus physics, or radiation physics in this study. We use  
206 the nonlinear backscatter and anisotropy (NBA) scheme (Kosović, 1997; Mirocha et al., 2010)  
207 to model subgrid-scale (SGS) mixing in the LES and mesoscale domain respectively. In the  
208 LES sub-domain, the Monin-Obukhov similarity theory is used to parameterize the surface layer  
209 (surface layer option 1 (Jiménez et al., 2012; Monin and Obukhov, 1954)).

210

<b>Label</b>	<b>Amplitude</b> $F_{xy}$ (kgs <sup>-4</sup> )	<b>Amplitude</b> $F_z$ (kgs <sup>-4</sup> )	<b>Ktop</b> (value)	<b>Height</b> (meters)
No-SCPM	—	—	—	—
Periodic	—	—	—	—
Ktop34L	1,000	1,500	34	307
Ktop54L	1,000	1,500	54	609
Ktop88L	1,000	1,500	88	1607
Ktop88M	2,000	4,000	88	1607
Ktop34H	5,000	10,000	34	307
Ktop54H	5,000	10,000	54	609
Ktop88H	5,000	10,000	88	1607

Table 1: The table shows a list of simulations performed in this study using different Ktop values as well as the maximum amplitude of perturbations in both horizontal and vertical directions. It also shows the periodic and No-SCPM simulations used to compare the results of the SCPM-M cases.

## 211 **2.2 Experimental set-up**

### 212 **2.2.1 SCPM Simulations**

213 In this study, we apply momentum perturbations to  $8 \times 8 \times 1$  grid point cells from the surface up  
214 to the 34<sup>th</sup>, 54<sup>th</sup>, and 88<sup>th</sup> pressure level along the inflow boundary of the LES domain (denoted  
215 as Ktop34, Ktop54, and Ktop88 respectively). The vertical extent of these perturbations is  
216 307 m, 609 m, and 1,607 m, respectively. These extents correspond to heights halfway between  
217 the surface and the capping boundary layer, the height of the capping boundary layer, and the  
218 top of the domain. We also vary the perturbation amplitude. Simulations with low amplitude  
219 perturbations ( $F_{xy} = 1000 \text{ kgs}^{-4}$ ;  $F_z = 1500 \text{ kgs}^{-4}$ ) are denoted as Ktop34L, Ktop54L, and  
220 Ktop88L), and simulations with high amplitude perturbations ( $F_{xy} = 5000 \text{ kgs}^{-4}$ ;  $F_z = 10000$   
221  $\text{kgs}^{-4}$ ) as Ktop34H, Ktop54H, and Ktop88H (Table 1).

222 In addition, we would like to investigate whether forces lower than the higher amplitude  
223 perturbations are able to reduce the fetch in TKE generation. Therefore, we apply a combination  
224 of forces that have forcing amplitude between the higher and lower amplitude perturbations. We  
225 refer to these forces as medium amplitude perturbations. For medium amplitude perturbations  
226 ( $F_{xy} = 2000 \text{ kgs}^{-4}$ ;  $F_z = 3000 \text{ kgs}^{-4}$ ), we only perform a simulation for the Ktop88 case  
227 (denoted by Ktop88M in Table 1) for the following reason. This case involves the application of  
228 forces above the CBL height. This, in turn, gives us the opportunity to examine the impact of  
229 these forces throughout the entire inner domain, i.e., both above and below the CBL height. In  
230 contrast, applying medium amplitude perturbations at other heights (as in the case of Ktop34  
231 and Ktop54) is devoid of this opportunity.

### 232 **2.2.2 No-SCPM and Periodic Simulations**

233 In addition to the SCPM simulations described above, we also perform a simulation where no  
234 perturbations are applied, the No-SCPM simulation. The domain configuration and simulation  
235 time for this simulation are the same as for the SCPM-M simulations.

236 We also compare SCPM simulations against a simulation where turbulence is developed  
237 through the use of periodic boundary conditions, i.e. output conditions at the outflow become  
238 input conditions at the inflow. We do not use nested domains for the periodic simulation. Rather,  
239 a single LES domain with 600 grid cells in  $X$  direction and 600 grids in  $Y$  is used. The domain  
240 size is 7.2 km by 7.2 km. We also use 88 vertical eta levels with the top level at 1,608 m (ztop).  
241 The input sounding remains the same as in SCPM-M simulations. The time step for integration

242 is 0.05 seconds and the outputs for the LES domain are stored every minute. Both periodic and  
 243 No-SCPM simulations are summarized in Table ref T1 SCPM M.

<b>WRF Parameters</b>	<b>Values</b>
WRF version	V4.1.3
Duration of simulation	6 hours
Spin-up time	4 hours
Duration of SCPM-M	2 hours
Horizontal resolution	240 m (parent domain), 12 m (LES domain)
Vertical resolution	88 vertical eta levels
Grid spacing	480x480 (parent domain), 961x481 (LES domain)
Grid spacing (periodic)	600x600
Time step	0.5 s (parent domain), 0.01 s (LES domain)
Parent time step ratio	50

Table 2: The table shows the WRF model configuration and the summary of general information on the domain design used in this study.

### 244 **2.3 Analysis Methods**

245 In order to calculate mean and turbulent statistics, we use standard turbulence decomposition,  
 246 where  $u' = U - \bar{U}$ ,  $v' = V - \bar{V}$ ,  $w' = W - \bar{W}$ , and  $\theta' = \theta - \bar{\theta}$  where  $\bar{\theta}$ . Here  $U$ ,  $V$ , and  
 247  $W$  are the instantaneous velocity components,  $\theta$  is the potential temperature, over-bars denote  
 248 time averaging, and primes denote fluctuations from the mean. We choose time averaging to  
 249 evaluate the temporal behavior and variations of mean fields to calculate perturbations in these  
 250 fields in our study. The purpose is to capture the average behavior of the fields over a certain  
 251 time period by using temporal averaging and varying perturbations of the fields, which could  
 252 potentially show interesting patterns and trends. The wind speed is calculated as  $\sqrt{\bar{U}^2 + \bar{V}^2}$   
 253 with an averaging time of the last 30 minutes of simulation i.e., from 19:30 Z to 20 Z UTC (1:30  
 254 p.m. to 2 p.m. Central time). The heat flux is given by  $\overline{w'\theta'}$  and momentum flux is given by  
 255  $\overline{w'u'}$ .

256 The  $\bar{e}$  is the TKE, defined as:

$$\bar{e} = 0.5(\overline{u'u'} + \overline{v'v'} + \overline{w'w'}) \quad (1)$$

257 The turbulent kinetic energy (TKE) budget equation is given by Stull (1988):

$$\frac{\partial \bar{e}}{\partial t} + \bar{U}_j \frac{\partial \bar{e}}{\partial x_j} = \delta_{i3} \frac{g}{\theta_v} \overline{u'_i \theta'_v} - \overline{u'_i u'_j} \frac{\partial \bar{U}_i}{\partial x_j} - \frac{\partial \overline{u'_j e}}{\partial x_j} - \frac{1}{\bar{\rho}} \frac{\partial \overline{u'_i p'}}{\partial x_i} - \epsilon \quad (2)$$

258 The first and second terms on the left-hand side (LHS) of equation 2 represent local storage  
 259 or the tendency of TKE and the advection of TKE by mean wind, respectively. The terms on the  
 260 right-hand side (RHS) of equation 2 in order from left to right represent the buoyant production  
 261 or consumption term, a mechanical or shear production term, the turbulent transport of TKE,  
 262 a pressure correlation term, and the viscous dissipation of TKE, respectively (Stull, 1988).

263 The TKE budget equation after assuming horizontal homogeneity, neglecting subsidence, and  
 264 choosing a coordinate system that is in the direction of mean wind, is simplified as:

$$\frac{\partial \bar{e}}{\partial t} = + \frac{g}{\theta_v} \overline{w' \theta'_v} - \overline{u' w'} \frac{\partial \bar{U}}{\partial z} - \frac{\partial \overline{w' e}}{\partial z} - \frac{1}{\bar{\rho}} \frac{\partial \overline{w' p'}}{\partial z} - \epsilon \quad (3)$$

265 Using these concepts and equations, we compute TKE, heat, and momentum fluxes, as well  
 266 as TKE budget terms associated with buoyancy, shear, transport, and pressure correlation for  
 267 all simulations outlined in Table 1. In the next section, we present and discuss the results of this  
 268 analysis.

## 269 3 Results and Discussion

### 270 3.1 Turbulent kinetic energy (TKE)

#### 271 3.1.1 Spatial variation of TKE

272 TKE is a measure of the intensity of turbulence. We calculate TKE for all simulations (Table 1)  
 273 and compare its variation over height ( $z$ ) and streamwise distance ( $x$ ) (Figure 1). The distance  
 274 from the inflow boundary at which turbulent fluctuations start to develop is called fetch (Mazzaro  
 275 et al., 2017, 2019). We observe that for simulations without momentum perturbation (No-  
 276 SCPM), turbulence begins to develop 5,000 m into the domain, with a significant fetch, and a  
 277 realistic representation of fully developed turbulent structures only appears in the last 25% of  
 278 the domain. After applying SCPM-M, the fetch is reduced significantly for all perturbed cases.

279 For high amplitude perturbations (Figure 1b-d), the fetch is diminished, but the maximum  
 280 of TKE is present along the inflow boundary and near the boundary layer top. For Ktop54H and

281 Ktop88H, positive values of TKE extend above the boundary layer, an artifact related to the high  
282 perturbation height and amplitude (Figure 1c) and Figure 1d). Furthermore, for Ktop34H, the  
283 TKE maximum is present near the bottom of the domain, near the surface and most importantly,  
284 the fetch has reduced significantly (Figure 1b).

285 In the case of lower and medium amplitude perturbations (Figure 1(e-h)), the TKE maxima  
286 near the boundary layer are not present. We also observe that the rate at which the TKE increases  
287 with the downwind  $x$  direction is similar for the medium and lower amplitude perturbations but  
288 not the same as the No-SCPM case (Figure 1a).

289 These spatial patterns highlight that the vertical and horizontal extent of inflow perturbations  
290 can influence the underlying turbulence evolution. Moreover, SCPM-M produces a vertical profile  
291 of TKE that spans the boundary layer more rapidly than without the perturbations. In addition,  
292 tuning the amplitude of the perturbation helps minimize the fetch to fully develop the TKE. Here,  
293 the term “fully developed” we do not mean that TKE has reached the exact same value, but  
294 rather the same order of magnitude. However, if the height of perturbations approaches or  
295 exceeds the boundary layer, this leads to artifacts in the flow field above the boundary layer  
296 height.

### 297 **3.1.2 Fetch**

298 In boundary-coupled simulations using inflow data that does not contain resolved turbulence  
299 at the time and space scales of the LES discretization (e.g. from a mesoscale simulation),  
300 the development of resolved-scale turbulence generally requires a long fetch. We compare the  
301 variation of Y-averaged TKE over height and longitude in the  $y$  and  $x$  axes respectively (at  
302 two heights, 10 m, and 53 m, Figure 2) from the perturbed cases and the periodic simulation to  
303 investigate the extent of the fetch. The distance from the inflow boundary at which the TKE  
304 from the SCPM-M simulations becomes comparable to the TKE obtained from the periodic  
305 simulation can be used as a rough estimator for the fetch. The fetch required to fully develop  
306 turbulence is referred to as ‘required fetch’ hereafter.

307 We observe that the required fetch is the longest for No-SCPM simulation (Figure 2a). At  
308 10 m height, the required fetch for the No-SCPM case is around 9,000 m, and at 53 m the fetch  
309 is around 7,200 m (Figures 2a-d). Before the fetch is fully established, the TKE increases to an  
310 unrealistically high level as indicated by the large departure from the periodic case.

311 However, after applying SCPM-M, the required fetch is reduced significantly. At both 10 m  
312 and 53 m, the TKE is fully developed around 2,000 m for all perturbed cases as shown in Figure 2.

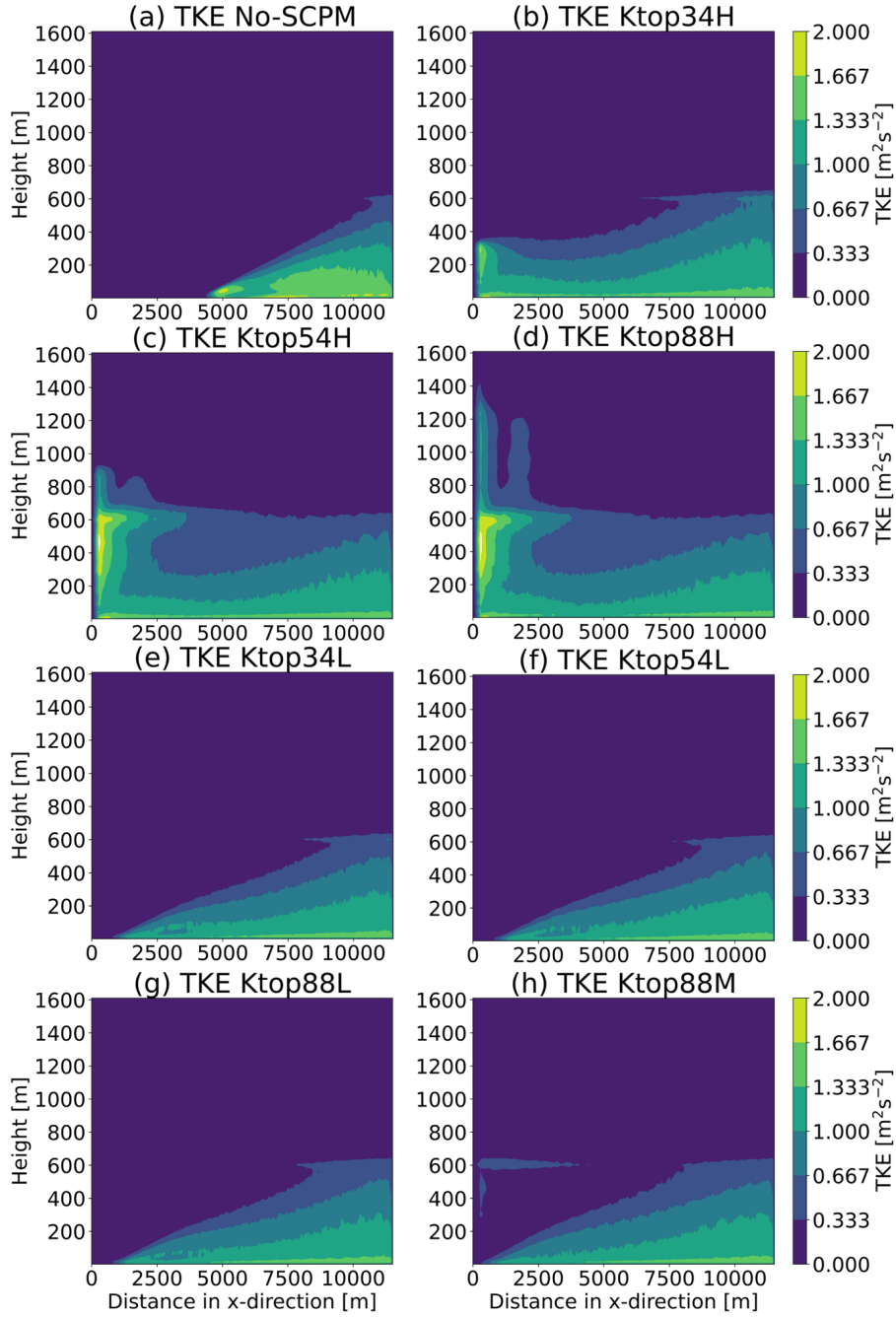


Figure 1: Y-averaged TKE ( $m^2/s^2$ ), computed over the entire inner domain, compared between simulations with and without momentum perturbation with different perturbation amplitudes and vertical extents with panels (a) No-SCPM, (b) Ktop34H, (c) Ktop54H, (d) Ktop88H, (e) Ktop34L, (f) Ktop54L, (g) Ktop88L, and (h) Ktop88M as shown in Table 1.

313 Quantitatively, we find that the TKE reaches 80% of its steady-state magnitude at 2000 m from  
 314 the inlet boundary in the case of SCPM-M simulations when compared to the periodic simulation  
 315 (Figure 2). On the other hand, the No-SCPM scenario takes 5000 m to achieve the same level  
 316 of TKE. At the last quarter of the domain, starting at  $x = 9,600$  m, the TKE for the perturbed  
 317 cases is quite close to the periodic case. Therefore, we will use the last three-quarters of the  
 318 domain ( $x$  from 2,880 m to 11,520 m) to average over turbulence statistics subsequently reported  
 319 in this study. The TKE profiles averaged over the last quarter of the domain ( $x$  from 86,400 m to  
 320 11,520 m) will be reported only for reference in section 3.1.3. Furthermore, the TKE evolves over  
 321 time and space after applying SCPM-M. For instance, we can see this spatial evolution when we  
 322 compare the area-averaged TKE over the last quarter of the domain to the area average over  
 323 the last three-quarters of the domain. The former is much closer to the periodic value than the  
 324 latter. For more information on the effects of the spatial averaging domain on fluxes and TKE  
 325 budget terms, please see the supplementary material (Subsection S4.1).

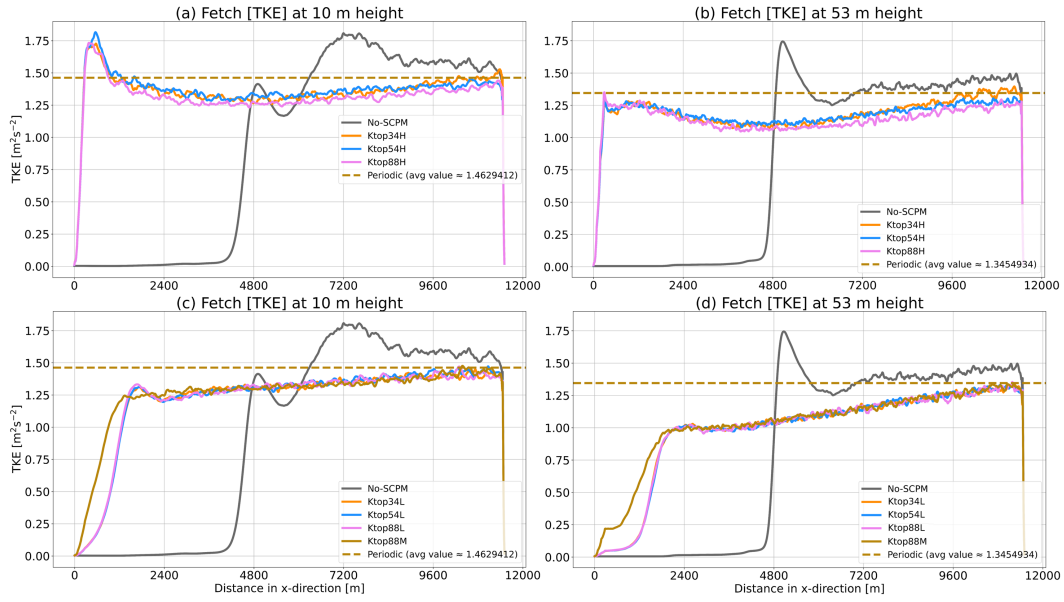


Figure 2: Fetch of Y-averaged TKE ( $m^2/s^2$ ), computed after applying momentum perturbation with higher, medium, and lower amplitudes as shown in (Table 1) and show fetch at (a) 10 m height for periodic, No-SCPM, and higher amplitude SCPM-M, (b) 53 m height for periodic, No-SCPM, and higher amplitude SCPM-M, (c) 10 m height for periodic, No-SCPM, and lower and medium amplitude SCPM-M, (d) 53 m height for periodic, No-SCPM, and lower and medium amplitude SCPM-M. These plots are generated for TKE that are Y-averaged over the entire inner domain.

### 326 3.1.3 TKE profiles

327 Based on the discussion in the previous section 3.1.2, we compare the TKE profiles that are  
328 averaged over two different areas: three-quarters of the domain (overall  $y$  and  $x$  from 2,880 m to  
329 11,520 m) farthest away from the inflow (Figures 3 (a-b)), and last quarter of the domain (overall  
330  $y$  and  $x$  from 86,400 m to 11,520 m) farthest from the inflow (Figures 3 (c-d)). We observe that  
331 applying SCPM-M produces TKE closer to the periodic case regardless of the extent of its  
332 application (Figures 3(a-d)).

333 As it is observed in Figure 3, the TKE is highest near the surface and decreases with height in  
334 all SCPM-M simulations and as well as in the case of No-SCPM. Up to 200 m, the TKE is similar  
335 for all the perturbed cases as well as the periodic case, while the TKE for the No-SCPM case  
336 is lower, when the TKE is area-averaged over the last three-quarters of the domain (Figures 3a-  
337 b). However, between 300 m and up to the CBL height, SCPM-M cases with higher amplitudes  
338 (Ktop34H, Ktop54H, and Ktop88H) are closer to the periodic case; while No-SCPM shows the  
339 largest deviation from the periodic case (Figures 3a-b). When the last quarter area-averaged  
340 profiles are compared (Figures 3c-d), we find that the TKE is highest for No-SCPM case below  
341 300 m and it decreases sharply above 300 m, deviating the most from the periodic case. However,  
342 the SCPM-M cases are closer to the periodic case for all heights. In addition, we also observe  
343 that the medium and lower amplitude SCPM-M cases are almost equal in magnitude throughout  
344 the domain (Figure 3d). From the high amplitude SCPM-M cases, the TKE for the Ktop34H  
345 is closest to the periodic case above 300 m (Figure 3c). It is important to note that the effect  
346 of momentum perturbation is not only to enhance TKE but rather to adjust TKE closer to the  
347 appropriate levels at all heights within the CBL. Therefore, even though SCPM-M is shown to  
348 correct less than half the bias while TKE is evolving, measured as the difference in TKE values  
349 between the periodic simulation and the No-SCPM simulation, for a significant portion of the  
350 CBL, it performs better than No-SCPM for a significant portion of the CBL.

## 351 3.2 Mean and instantaneous flow features

### 352 3.2.1 Instantaneous flow features

353 Figure 4 shows the instantaneous  $U$  component of velocity at two-thirds and half of the CBL  
354 height (211 m and 391 m, respectively) for simulations without SCPM and the SCPM applied to  
355 three different vertical extents. These velocities are shown at the last instant of the simulation  
356 period i.e., at 20 Z (UTC) for the nested LES domain. As observed in Figures 1,2, and 3, and in

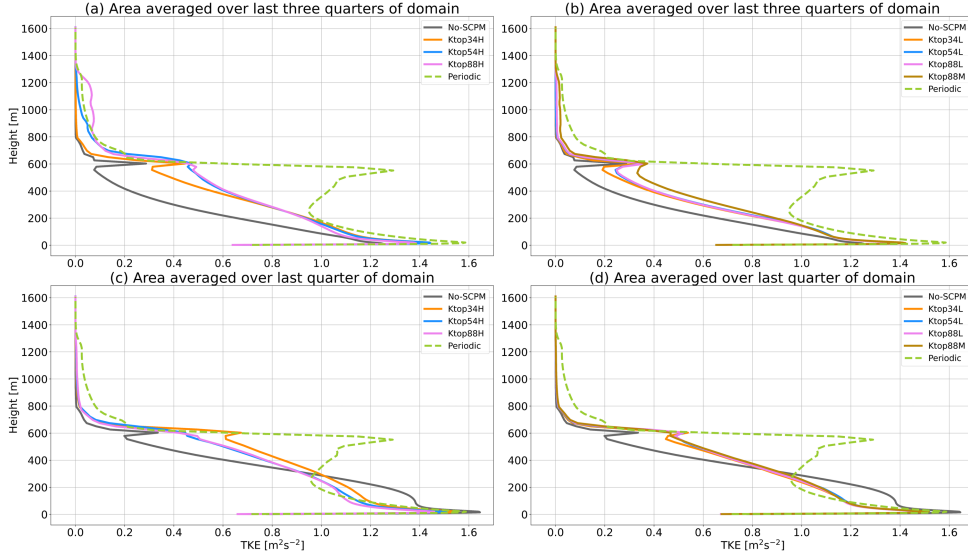


Figure 3: Area-averaged TKE ( $m^2/s^2$ ) profiles, computed for the inner domain after applying momentum perturbation with higher amplitude (Table 1) in the right panels and lower & medium amplitudes (Table 1) in the left panels, respectively. Profiles (a) and (b) show TKE values that are area-averaged over the last three-quarters of the domain, i.e., overall  $y$  and  $x$  from 2,880 m to 11,520 m for (a) Periodic, No-SCPM, and high amplitude SCPM-M (Ktop34H, Ktop54H, and Ktop88H); (b) Periodic, No-SCPM, and low and medium amplitude SCPM-M (Ktop34L, Ktop54L, Ktop88L, and Ktop88M). While, panels (c) Periodic, No-SCPM, and high amplitude SCPM-M (Ktop34H, Ktop54H, and Ktop88H), and (d) Periodic, No-SCPM, and low and medium amplitude SCPM-M (Ktop34L, Ktop54L, Ktop88L, and Ktop88M) are the TKE profiles that are area-averaged over only the last quarter of the domain, i.e., overall  $y$  and  $x$  from 86,400 m to 11,520 m.

357 previous studies, such as Mazzaro et al. (2017, 2019), a large fetch is required for the No-SCPM  
 358 simulation. The fetch is reduced significantly whenever perturbations are applied, regardless of  
 359 the extent and amplitude of the applied momentum perturbation.

### 360 3.2.2 Mean wind speed profiles

361 We find that the time and area-averaged (over the last 30 minutes of simulation for the last  
 362 three-quarters of the domain) vertical profiles of the wind speed for the different simulation  
 363 cases have a logarithmic profile near the surface layer up to the height of 200 m (Figure 5a).  
 364 In this study, we are interested in the lower atmospheric boundary layer (200 m), focusing on  
 365 applications such as wind energy. We used the term “surface layer” as 10-20% of the boundary  
 366 layer height. Under convective conditions, the profiles of mean velocity would not be perfectly  
 367 logarithmic, but one can use Monin-Obukhov Similarity Theory (MOST) to obtain stability

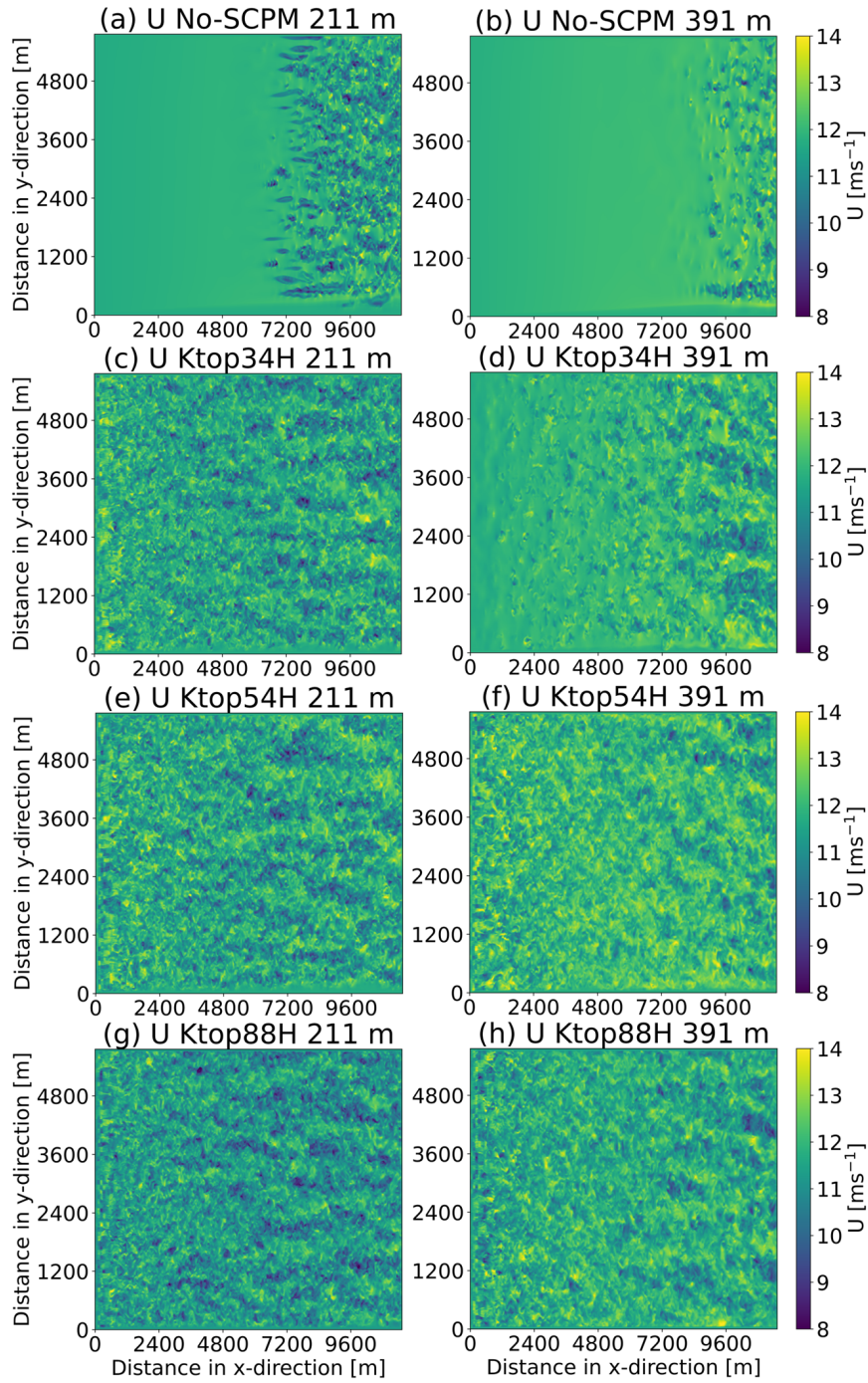


Figure 4: Instantaneous  $U$  component of velocities ( $\text{ms}^{-1}$ ), computed at two different heights that are at half (level=27,  $z=211$  m) and at two-thirds (level=37,  $z=391$  m) of the boundary layer height for (a-b) No-SCPM, (c-d) Ktop54H (e-f) Ktop54H (g-h) Ktop88H. The color bar corresponds to the magnitude of velocity for panels (a) to (h).

368 correction functions. However, in this case, since very mildly unstable conditions are used, we  
 369 did not focus on stability corrections. The extent and amplitude of inflow perturbations have a  
 370 small effect on the wind speed profiles. Between 100 m to 500 m, the wind speed for the No-SCPM  
 371 case is higher as compared to the other perturbed cases. Between 100 m to 500 m, the lowest  
 372 wind speed is observed for the periodic simulation (dashed line) followed by the Ktop88H case  
 373 (purple line) Figure 5(a-b), compared to the other cases. Wind speed profiles for the lower and  
 374 medium SCPM-M cases are similar to each other but lower than the No-SCPM case up to about  
 375 500 m. We evaluated the model's capacity to accurately represent the atmospheric conditions  
 376 and enhance our confidence in the results by comparing the model results with the tower data  
 377 that is currently available in the form of observations from the SWiFT site. We compare the  
 378 observational wind speed (Figure 7a) and potential temperature (Figure 7b) profiles with model  
 379 results at three different instances i.e., 18 Z, 19 Z, and 20 Z 7. Figure 7(a-b) shows reasonable  
 380 agreement between the sounding and model wind speed and very good agreement for potential  
 381 temperature respectively, for the lower 200 m of the atmosphere for all three times.

### 382 **3.2.3 Velocity variance statistics**

383 In order to examine the contributions of the velocity variance components ( $\sigma_u^2$ ,  $\sigma_v^2$ ,  $\sigma_w^2$ ) to the  
 384 TKE, we area-average them over the last three-quarters of the domain and compute in Figure 6.  
 385 The notations with primes and overbars for variance are indicated with sigmas and subscripts.  
 386 Similar to the TKE profiles in Figure 3, all three velocity variances are higher for the SCPM-M  
 387 cases compared to the No-SCPM case. The  $\sigma_w^2$  is higher for the Ktop34H case around 200 m.  
 388 Just below the CBL height of 600 m, the  $\sigma_u^2$  and  $\sigma_v^2$  are higher for Ktop88H compared to the  
 389 other cases.

### 390 **3.3 Fluxes of sensible heat and momentum**

391 Similar to the other turbulence statistics, the fluxes of sensible heat ( $\overline{w'\theta'}$ ) and momentum ( $\overline{u'w'}$ )  
 392 are averaged over the last three-quarters of the domain and plotted in Figure 8. We observe that  
 393 below 200 m, the fluxes of sensible heat and momentum are higher for the No-SCPM case as  
 394 compared to the SCPM-M cases (Figure 8). This could be attributed to unrealistically high  
 395 levels of TKE in the No-SCPM case in the last two-quarters of the domain, as observed in Figure  
 396 2. Above 200 m, the sensible heat flux for the SCPM-M cases is similar to the No-SCPM case

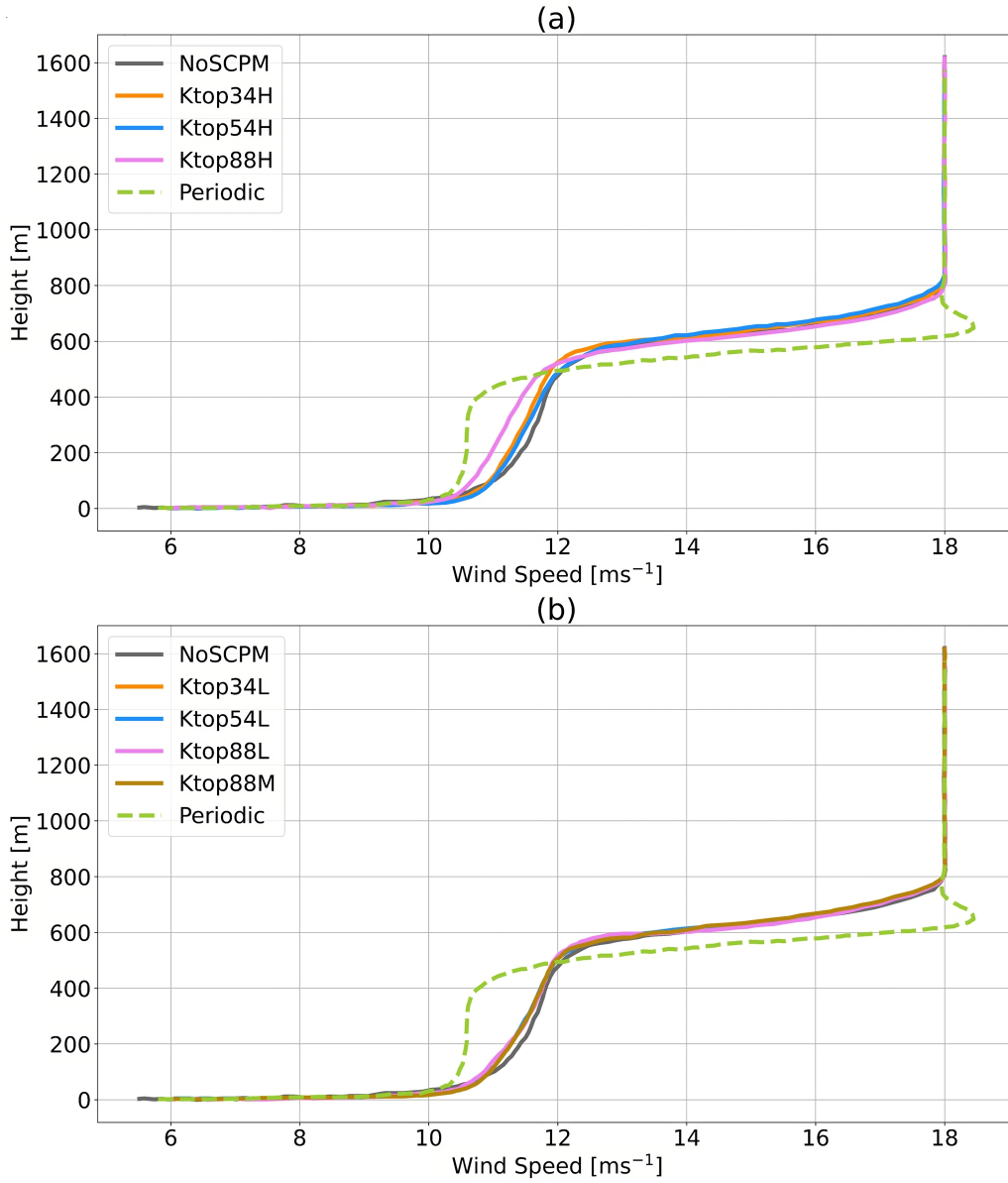


Figure 5: Wind speed (ms<sup>-1</sup>) area-averaged over three-quarters of the domain (all  $y$  and  $x$  from 2,880 m to 11,520 m) for all the cases as shown in Table 1 for (a) higher, (b) lower and medium amplitude SCPM-M as well as No-SCPM and periodic simulation. The wind speeds are generated from the last 30 minutes of the simulation time period i.e., from 19 Z (UTC) to 20 Z (UTC) and for the top of the entire simulation inner domain up to 1608 m.

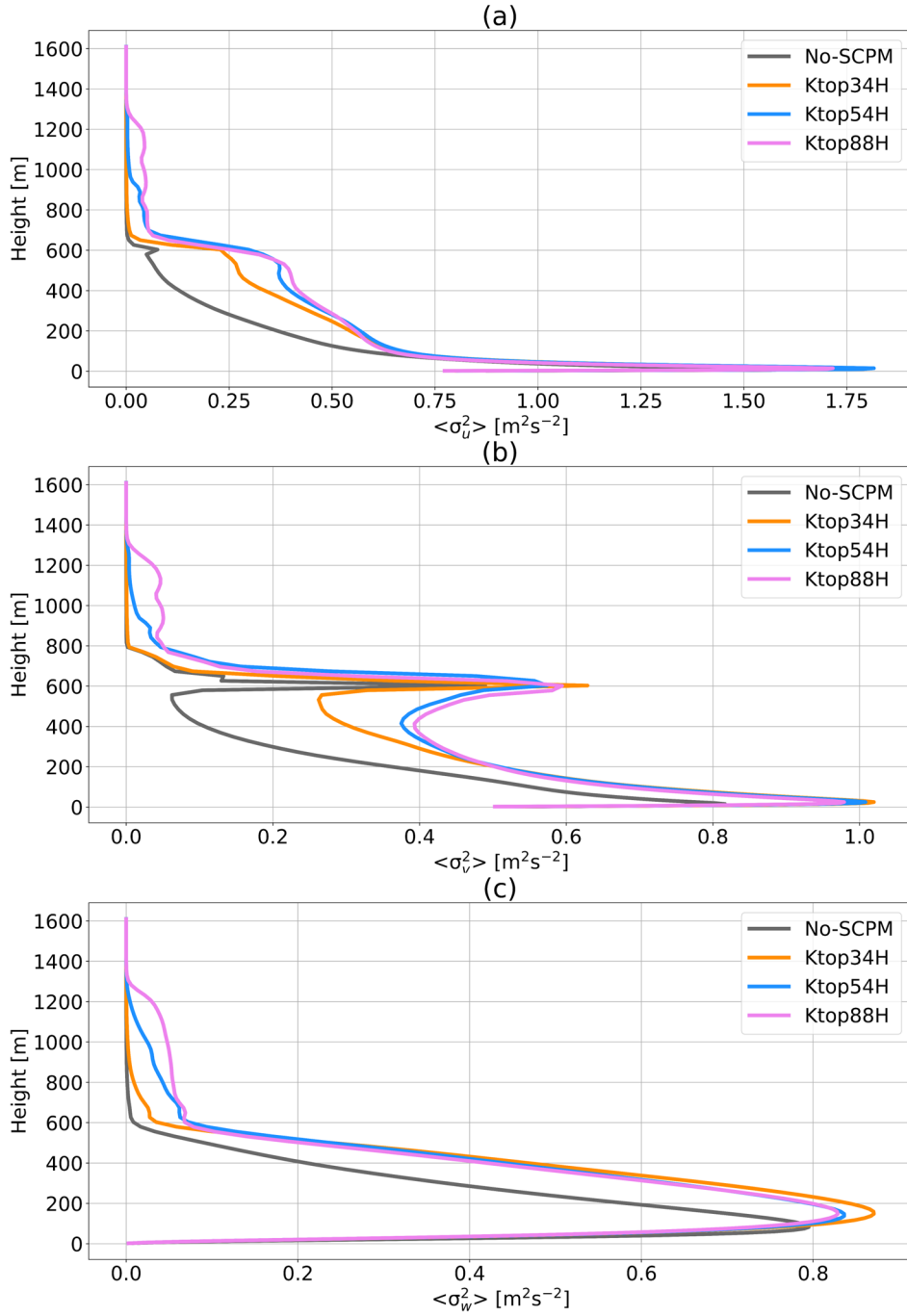


Figure 6: Area-averaged (a)  $\langle \sigma_u^2 \rangle$ , (b)  $\langle \sigma_v^2 \rangle$ , and (c)  $\langle \sigma_w^2 \rangle$  over three quarters of the domain (all  $y$  and  $x$  from 2,880 m to 11,520 m) for No-SCPM, Ktop34H, Ktop54H, & Ktop88H. These results are shown from the last simulation period at 20 Z and for the top of the entire simulation inner domain up to 1,608 m. The angular brackets denote area averaging.

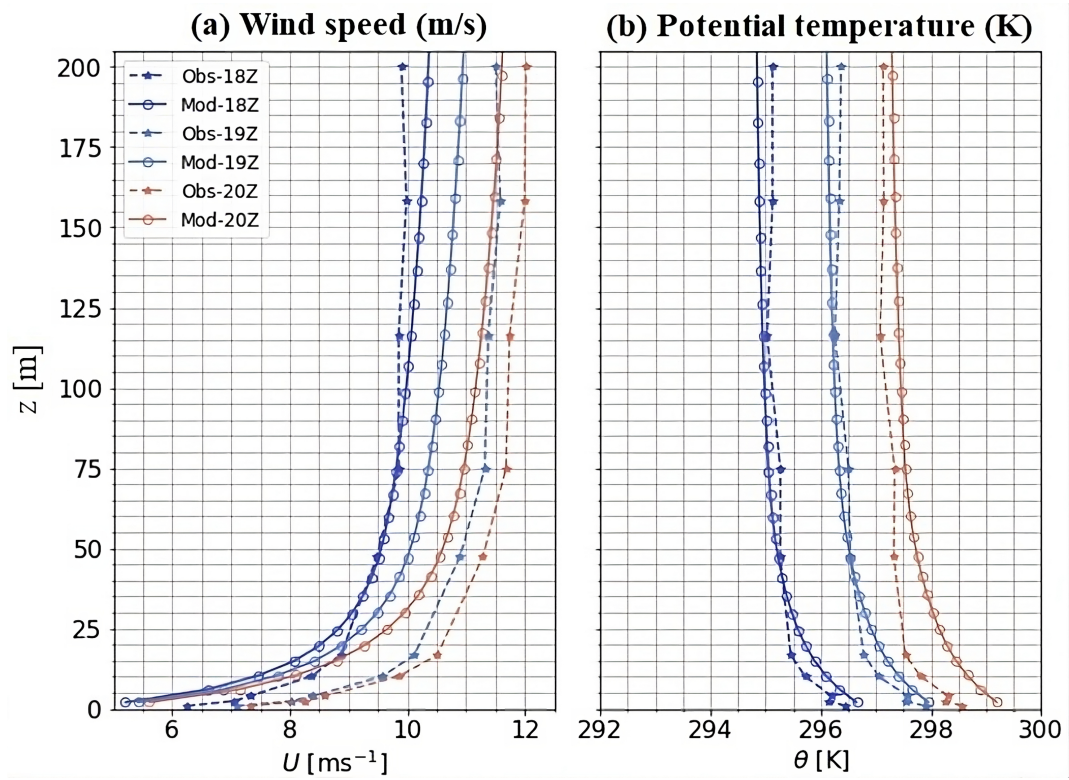


Figure 7: Profiles of domain-averaged (a) wind speed and (b) potential temperature at hours 18, 19, and 20 Z (UTC) during assessment (18-20Z) periods, versus centered 30-minute-averaged quantities observed at the SWiFT.

397 (Figure 8(a-b)). However, the momentum fluxes are higher for the SCPM-M cases than the  
398 No-SCPM (Figure 8c-d) case above 200 m.

399 Among the SCPM-M cases, the Ktop34H has a higher magnitude of sensible heat flux than  
400 the other cases (Figure 8a). Here, we use the SI prefix 'k' for 'kilo' for the heat flux unit as it has  
401 a high magnitude during a convective case. The lower and medium amplitude SCPM-M cases  
402 are similar in the sensible heat flux throughout the domain (Figure 8b). For the momentum  
403 flux, all high amplitude SCPM-M cases (Figure 8c) and all the low and medium amplitude cases  
404 (Figure 8d) are similar to each other.

405 At the top of the inversion layer, Ktop34H has the highest entrainment flux (this is where the  
406 'potentially' warmer air is entrained into the CBL), as indicated by the strongly negative sensible  
407 heat flux at the top of the CBL for Ktop34H. Ktop88H and Ktop54H simulations produce similar  
408 entrainment fluxes of heat from above into the CBL. This is due to turbulence being artificially  
409 excited near and above the top of the CBL.

410

### 411 **3.4 Turbulent kinetic energy budget**

412 Since sensible heat flux and momentum flux contribute to TKE generation, the components of  
413 the budget equation for the TKE are worth investigating for the simulated cases. Therefore,  
414 individual terms of the TKE budget are discussed in this section. Figure 9 shows the  $y$ -averaged  
415 components of the TKE budget for the No-SCPM (left column) and the Ktop34H case (right  
416 column). We focus our discussion on the Ktop34H case because (1) additional entrainment at  
417 the capping inversion level is very low compared to the other cases, and (2) the reduction in fetch  
418 is significant. The other high amplitude cases, while reducing the fetch, generate additional  
419 entrainment at the CBL height. In contrast, the low amplitude and medium amplitude cases are  
420 less efficient in the fetch reduction.

421 The  $y$ -averaged TKE budget terms for other SCPM-M cases are plotted in the supplementary  
422 material (Figure S14). Vertical profiles of the TKE budget terms, averaged over the three quarters  
423 farthest from the inflow of the domain are shown in Figure 10 for all SCPM-M cases as well as  
424 the No-SCPM case.

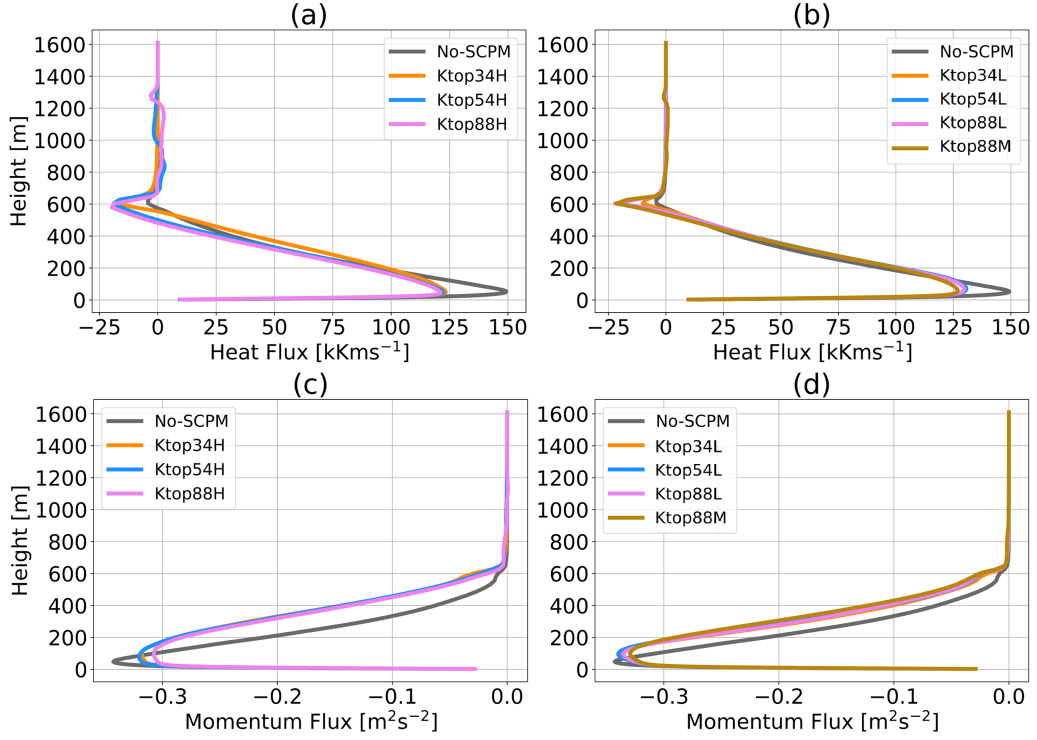


Figure 8: Heat flux  $(\overline{w'\theta'})$  profiles after applying momentum perturbation (SCPM-M) with (a) higher amplitudes of forces, as shown in (Table 1), (b) lower & medium amplitudes of forces; momentum flux  $(\overline{u'w'})$  with (c) higher amplitudes of forces, and (d) lower & medium amplitudes of forces. In addition, these profiles are computed in a way that the heat flux  $(\overline{w'\theta'})$  and momentum flux  $(\overline{u'w'})$  are area-averaged over the last three-quarters of the inner domain i.e., overall  $y$  and  $x$  from 2,880 m to 11,520 m and are shown for the top of the entire simulation inner domain up to 1608 m.

425 **3.4.1 Buoyancy Term**

426 The  $y$ -averaged buoyancy term  $(g/\bar{\theta})\overline{w'\theta'}$  for the No-SCPM and Ktop34H cases are plotted in  
427 Figure 9a and b.

428 We observe that for the No-SCPM case, the buoyancy term starts developing from the center  
429 of the  $x$  axis (Figure 9a). However, the fetch for the buoyancy term is reduced significantly  
430 for the perturbed cases (Figure 9b) and Figure S14). For Ktop54H and Ktop88H, the fetch  
431 is reduced appreciably, however, additional entrainment can be observed near the CBL height  
432 (Figure S14a-b). In general, lower amplitude perturbations reduce the fetch and do not create  
433 additional entrainment. Another important point to note is that the application of momentum  
434 perturbation (SCPM-M) is sufficient to modify the buoyancy term, without requiring perturbing  
435 the temperature field, as demonstrated by Mazzaro et al. (2019). This could be explained by  
436 the fact that the force-perturbation method generates additional  $w'$  fluctuations in the turbulent  
437 field, which excites the vertical sensible heat flux  $\overline{w'\theta'}$  as well.

438 As observed in Figure 10a-b, the vertical profile of the buoyancy term follows the same trend  
439 of the sensible heat flux profiles as shown in Figure 8a-b.

440 **3.4.2 Shear Term**

441 The momentum flux  $\overline{u'w'}$  is negative as momentum is absorbed towards the ground, and therefore  
442 the term  $-\overline{u'w'}(\partial U/\partial z)$  is positive and a source of TKE. Without applying momentum pertur-  
443 bation, we find that WRF-LES is unable to generate shear production (Figure 9c) from the very  
444 beginning of the lateral boundary and thus results in a long fetch before turbulence develops, as  
445 observed in the plan-view plots of velocities (Figure 4 and Figure S12). Since applying SCPM-M  
446 reduces the fetch in velocity generation, in a similar fashion, the fetch in shear production is also  
447 reduced because it is a combination of both (u and w) quantities  $(-\overline{u'w'}(\partial U/\partial z))$ .

448 We find that SCPM-M with higher amplitudes reduces the fetch in shear production signif-  
449 icantly, as shown in Figure 9d. However, in Ktop54H and Ktop88H, strong shear production is  
450 observed at the beginning of the LES domain near the lateral boundary (Figure S15a-b). This  
451 can be attributed to the application of SCPM-M near and above the CBL, which produces super-  
452 fluous turbulent motions and ultimately contributes to strong shear production above the CBL.  
453 Furthermore, we observe a small to moderate intensity of shear production near the CBL height  
454 for the SCPM-M cases due to a strong  $\partial U/\partial z$  in the last quarter of the domain (Figure 9d).  
455 Other SCPM-M cases are shown in the supplementary materials. In other SCPM-M cases with

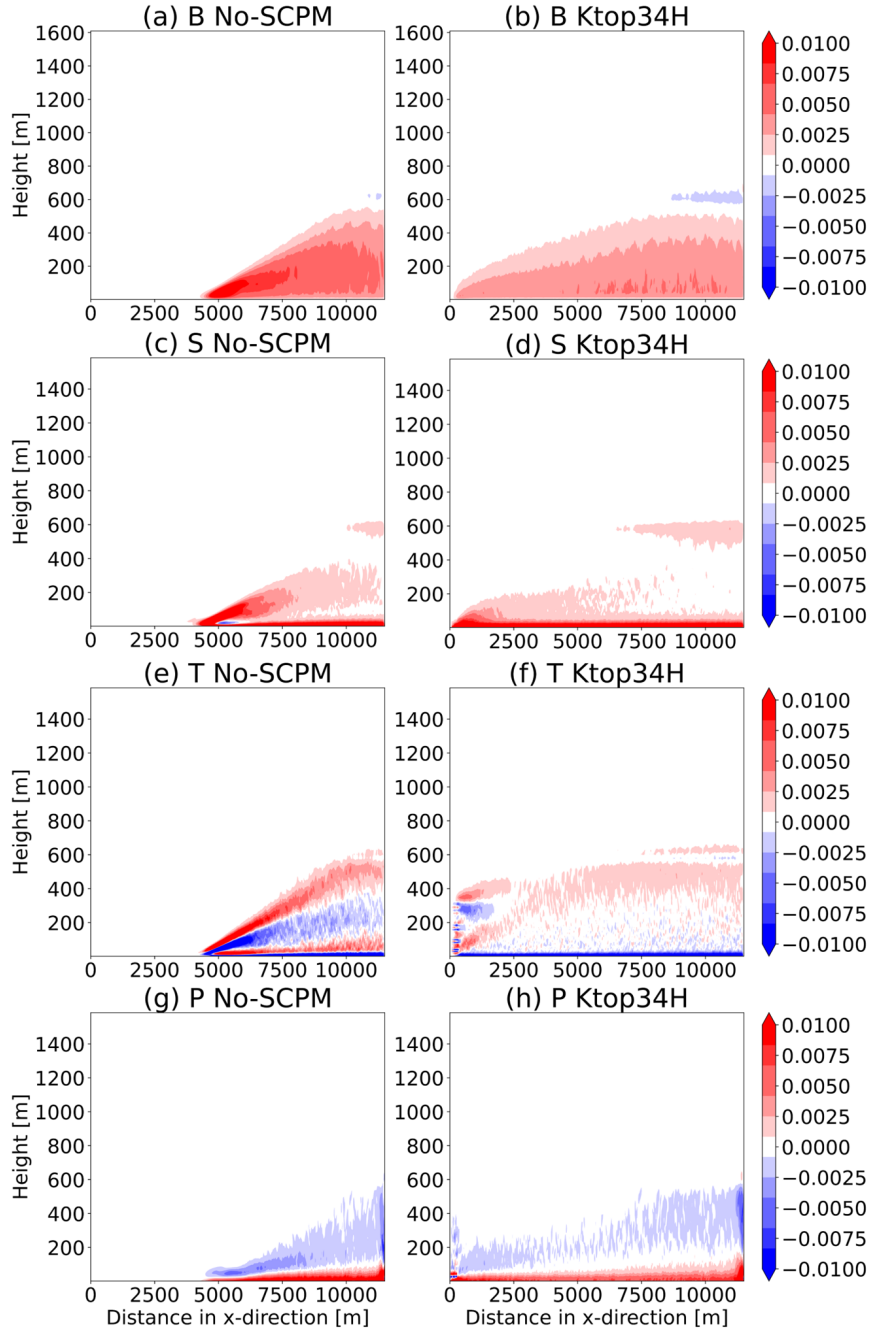


Figure 9: Y-averaged TKE budget terms after applying momentum perturbation following (Table 1), for the buoyancy term with (a) No-SCPM, (b) Ktop34H, for the shear production term with (c) No-SCPM (d) Ktop34H, for the turbulent transport with (e) No-SCPM (f) Ktop34H, and for the pressure correlation term with (g) No-SCPM, (h) Ktop34H. The color bar corresponds to the magnitude of TKE budget terms for panels (a) to (h). These plots are generated for TKE budget terms that are Y-averaged over the entire inner domain.

456 lower and medium amplitudes (Figure S15c-f), the fetch is reduced to a great extent without  
457 the generation of spurious motions near the lateral boundary at the beginning of the innermost  
458 domain.

459 Applying momentum perturbation within the LES domain contributes to maximum shear  
460 production near the surface in all the cases, as shown in Figure 10c-d. When compared to the  
461 No-SCPM case, the largest magnitude of shear production with SCPM-M is higher below the  
462 height of 200 m. There is a small but sharp jump in the shear term near the entrainment zone,  
463 regardless of the amplitudes of SCPM-M. Shear production reaches zero just above the CBL in  
464 all the SCPM-M cases. It diminishes completely at 650 m above the surface.

### 465 3.4.3 Turbulent Transport Term

466 In a planar homogeneous case without subsidence, the turbulent transport term in the TKE  
467 budget integrates over the domain height to null, indicating that TKE is transferred among  
468 horizontal planes (Stull, 1988). The  $\overline{w'e}$  is the major contributor to the turbulent transport term  
469 in the TKE budget equation. Here, we compare the  $y$ -averaged turbulent transport terms for  
470 different SCPM-M cases. Furthermore, the planar homogeneous assumption is on the boundary  
471 condition and land cover and it is not on the flow itself. In addition, even with the planar  
472 homogeneous flow boundary condition, the TKE needs space to develop.

473 Beyond  $x = 4,800$  m, gain due to turbulent transport ( $T > 0$ ) alternates with loss due to  
474 turbulent transport ( $T < 0$ ), as we ascend along the  $y$  - *axis* up to the CBL height in the No-  
475 SCPM case (Figure 9e). After applying SCPM-M, redistribution of the TKE starts at the  
476 beginning of the domain, as shown in Figure 9f (Figure S16a-f shows all the other cases for the  
477 sake of completion). Therefore, the fetch in the generation of the turbulent transport term is  
478 reduced significantly with SCPM-M. However, the SCPM-M cases with higher amplitude produce  
479 more entrainment near the inflow boundary as compared to the lower amplitude SCPM-M cases  
480 (Figure 9f and Figure S16a-f). Among the higher amplitude SCPM-M cases, Ktop34H produces  
481 lower entrainment (Figure 9f and Figure S16a-b). The entrainment is not produced for the lower  
482 amplitude SCPM-M cases (Figure S16c-e).

483 We also compute the profiles of the turbulent transport terms that are area-averaged over  
484 the last three-quarters of the domain (all  $y$  and  $x$  from 2,880 m to 11,520 m) for the simulations  
485 in this section (Figure 10e-f). We find that without the SCPM-M, the turbulent transport term  
486 increases up to 25 m and then continuously decreases up to 140 m, and then increases again up

487 to the bottom of the CBL. Finally, it ( $\overline{w'e}$ ) sharply decreases to null at the CBL top (Figure  
488 10e-f).

489 In the case of SCPM-M with higher amplitudes, the changes are more abrupt within the CBL  
490 and it approaches zero slightly above and below the CBL height (Figure 10e). Also, at higher  
491 amplitudes, their profiles are not exactly the same but are slightly different throughout the  
492 boundary layer up to the CBL top (Figure 10e). However, at the lower and medium amplitude  
493 SCPM-M cases, the turbulent transport terms are almost similar to the No-SCPM case above  
494 200 m (Figure 10f). Similar to the higher amplitude SCPM-M cases,  $\overline{w'e}$  reaches zero slightly  
495 above and below the CBL height (Figure 10f) for the lower and medium amplitude SCPM-M  
496 cases.

#### 497 **3.4.4 Pressure Correlation Term**

498 The pressure correlation term plays the role to redistribute TKE within the boundary layer.  
499 Additionally, in some cases, the pressure covariance does not dissipate energy but transfers it  
500 out of the boundary layer through gravity waves (Stull, 1988). Applying SCPM-M significantly  
501 reduces the fetch in the redistribution of TKE through the pressure correlation term, and the  
502 area-averaged profiles become smoother, as shown in Figure 10g and Figure S17a-f. The redis-  
503 tribution of TKE starts from the beginning of the domain with higher and medium amplitude  
504 perturbations, while it starts after  $x = 100$  m for the lower amplitude SCPM-M cases (Figure 9h  
505 and Figure S17a-f). In the case of Ktop54H and Ktop88H, we observe some spurious motions at  
506 the beginning of the domain (at the inflow boundary), as shown in Figure S17a-b.

507 We observe that applying momentum perturbation results in a higher magnitude of pressure  
508 correlation terms as compared to the No-SCPM case (Figure 10g-h). The magnitudes of these  
509 terms are slightly higher in the case of SCPM-M with higher amplitudes as compared to the  
510 SCPM-M cases with lower amplitudes (Figure 10g-h). The differences among higher and lower  
511 amplitude SCPM-M cases are not significant below 100 m as there are very low magnitudes of  
512 pressure fluctuations in the surface layer (i.e., the lowest 10% of the boundary layer).

#### 513 **3.4.5 Temporal evolution of TKE**

514 In this subsection, we investigate the evolution of the TKE with time to examine how long the  
515 effect of the momentum perturbation last after the perturbations are turned off. And then,

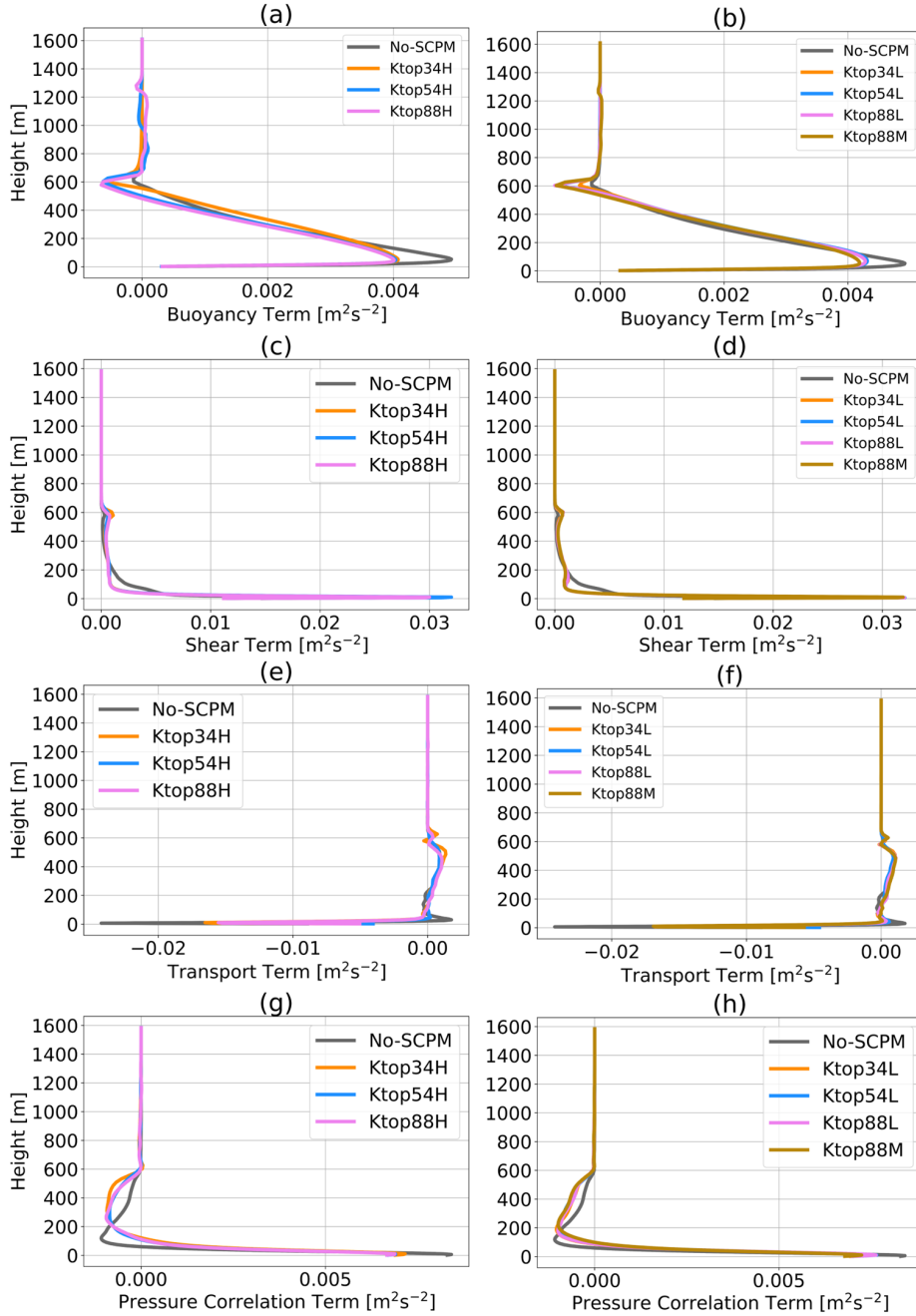


Figure 10: Area-averaged TKE budget terms over the last three-quarters of the domain, i.e., overall  $y$  and  $x$  from 2,880 m to 11,520 m after applying momentum perturbation for the buoyancy term with (a) higher amplitudes, (b) lower and medium amplitudes; for the shear production term with (c) higher amplitudes (d) lower and medium amplitudes; for the turbulent transport term with (e) higher amplitudes (f) lower and medium amplitudes; and for the pressure correlation term with (g) higher amplitudes, (h) lower and medium amplitudes. These plots are shown for the top of the inner domain from simulation (up to 1,608 m).

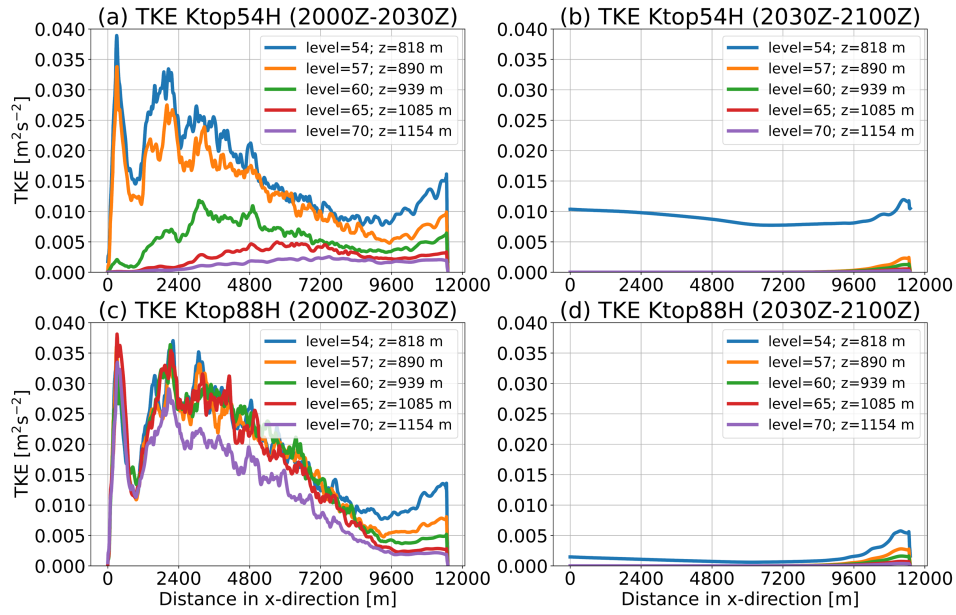


Figure 11: Y and time-averaged TKE ( $m^2/s^2$ ) profiles, computed at different heights in the atmosphere during an unstable case when momentum perturbation was turned off from (a) 20 Z to 20:30 Z (UTC) for Ktop54H, (b) 20:30 Z to 21:00 Z (UTC) for Ktop54H, (c) 20 Z to 20:30 Z (UTC) for Ktop88H, and (d) 20:30 Z to 21:00 Z (UTC) for Ktop88H in the different panels of the figure. These profiles are generated for buoyancy terms that are area-averaged over the entire inner domain.

516 if we want to maintain the sustained turbulence in the atmosphere, how frequently should we  
517 add these perturbations? We would like to clarify that it is neither about the lingering effects  
518 of perturbations nor about the application of perturbation during day and night. The SCPM-  
519 M simulations are performed for two hours, starting from 18Z (UTC) to 20Z (UTC). The  
520 application of external forces creates inertia, which is present for the next half an hour from  
521 the time when the momentum perturbation is stopped. As shown in Figure 11, although the  
522 magnitude of TKE that is generated due to inertia is low, it still remains finite from 20Z to  
523 20:30Z in the two cases, i.e., Ktop54H and Ktop88H (11(a and c)) (Ktop34H is not shown here  
524 but similar results are expected). Comparing the results after 20:30Z, Figure (11(a and c)) and  
525 Figure (11(b and d)), it is clear that the TKE dissipates and the effect of inertia is no longer  
526 present after 20:30Z (UTC).

## 527 4 Conclusions

528 In this work, we studied the impact of momentum perturbations, employed to generate turbu-  
529 lence in boundary-coupled LES simulations, on the turbulent kinetic energy (TKE) budget terms  
530 in an unstable boundary layer. It is well known that LES models that are used with periodic  
531 boundary conditions are capable of representing fully developed turbulence. However, turbulence  
532 representation is challenging in models that couple mesoscale and microscale domains or when  
533 conducting LES simulations with non-periodic conditions, such as in the presence of complex  
534 topography. Additional turbulence-generation techniques are needed in these instances. Several  
535 such techniques had been developed in the past, each one with its own advantages and disadvan-  
536 tages. Here, we implemented the stochastic cell perturbation technique in WRF-LES simulations  
537 to study the impact of turbulence generation on the TKE budget. We used an LES domain with  
538 a horizontal resolution of 12 m, which was nested within a mesoscale domain with a horizontal  
539 resolution of 240 m. Momentum perturbations were applied in the horizontal and vertical direc-  
540 tions at the inflow boundaries of the LES domain. We performed experiments where we varied  
541 perturbation amplitudes, as well as the heights to which the perturbations were applied with  
542 respect to the CBL height.

543 Applying SCPM-M accelerated turbulence generation, and significantly reduced the fetch,  
544 for all cases studied. Fetch reduction in coupled mesoscale-microscale atmospheric simulations  
545 results in lower computational costs of numerical experiments since a smaller domain would  
546 need to be resolved. While the magnitude of TKE produced was always higher for the SCPM-M  
547 cases than the No-SCPM case, we found that turbulence strength depended on the amplitude of  
548 perturbations, with higher-amplitude perturbations producing more turbulence than medium and  
549 lower-amplitude perturbations. Simulations with perturbations produced larger variances in the  
550 velocities up to the inversion layer than No-SCPM simulations. This also contributed to higher  
551 heat and momentum fluxes. We found that SCPM-M simulations provided comparable results  
552 with observations and that the model outputs are consistent with it. In summary, atmospheric  
553 stability plays a critical role in the generation and evolution of turbulence in the boundary layer.  
554 Stable atmospheric conditions suppress turbulence generation, while unstable conditions enhance  
555 it.

556 The perturbations also affected buoyancy production. SCPM-M simulations produced slightly  
557 more buoyancy than the No-SCPM case in the bottom and top third of the boundary layer,  
558 while buoyancy in the SCPM-M simulations was comparable to that in the No-SCPM case in

559 the middle third of the boundary layer. Shear production for the SCPM-M cases was higher  
560 than that for the No-SCPM case near the surface up to 35 m. Beyond this height, it decreased  
561 until it attained a value equal to the No-SCPM case at 200 m. Near the inversion layer, the shear  
562 production term in the SCPM-M case increased again due to entrainment-induced motions. The  
563 implementation of perturbations also impacted TKE redistribution through turbulent transport  
564 and pressure correlation terms. Our findings suggest that momentum perturbation enhances the  
565 coupling between shear and buoyancy-driven turbulence under unstable conditions.

566 Applying perturbations above the CBL height generated spurious turbulent structures at-  
567 tributed to additional entrainment at the top of the boundary layer, near the inversion layer. On  
568 the other hand, applying SCPM-M within the boundary layer or between the CBL height and  
569 the surface layer reduces additional entrainment-induced motions and computational costs.  
570 Based on the cases studied here, it can be concluded that applying momentum perturbations  
571 up to half the CBL height (the Ktop34H case) is optimal. This is because the Ktop34H case  
572 was characterized by significant fetch reduction and minimum generation of additional turbulent  
573 motions at the inversion layer.

574 The application of momentum perturbations to generate turbulence in boundary-coupled LES  
575 simulations can benefit a number of disciplines and applications, including but not limited to  
576 wind energy generation, wildfire modeling, cloud-top boundary layer research (applicable to off-  
577 shore wind), and dispersion problems. Accurate turbulence representation is also important for  
578 Uncrewed Aerial Vehicle research and weather forecasting. The results of this work will benefit  
579 these applications leading to an improved understanding of the physical Earth system models.

## 580 **Acknowledgements**

581 Funding for this work was provided by the U.S. DOE Office of Energy Efficiency and Renew-  
582 able Energy Wind Energy Technologies Office. M. Kumar acknowledges funding support from  
583 the Dean's Dissertation Fellowship award from the Henry Samueli School of Engineering at the  
584 University of California Irvine, and the Research Applications Laboratory visitor grant from the  
585 National Center for Atmospheric Research (NCAR). M. Kumar and T. Banerjee acknowledge  
586 support from the Subcontract agreement with Los Alamos National Laboratory, subcontract no.  
587 596883, agreement no. 351438. Banerjee also acknowledges funding support from the University  
588 of California Office of the President (UCOP) grant LFR-20-653572 (UC Lab-Fees); the National  
589 Science Foundation (NSF) grants NSF-AGS-PDM-2146520 (CAREER), NSF-OISE-2114740 (Ac-  
590 celNet) and NSF-CPS-2209695; the United States Department of Agriculture (USDA) grant

591 2021-67022-35908 (NIFA); and a cost reimbursable agreement with the USDA Forest Service 20-  
592 CR-11242306-072. The contribution of Branko Kosović was supported by the National Center  
593 for Atmospheric Research, which is a major facility sponsored by the National Science Founda-  
594 tion under Cooperative Agreement No. 1852977. William Lassman’s and Jeffrey D. Mirocha’s  
595 contributions were performed under the auspices of the U.S. Department of Energy by Lawrence  
596 Livermore National Laboratory under Contract DE-AC52-07NA27344. This research used re-  
597 sources provided by the Los Alamos National Laboratory Institutional Computing Program,  
598 which is supported by the U.S. Department of Energy National Nuclear Security Administration  
599 under Contract DE-AC52-06NA25396.

## 600 **Author Contributions**

601 **Mukesh Kumar:** Conceptualization, Methodology, Software, Data curation, Writing- Original  
602 draft preparation, Visualization, Investigation, Software, Validation, Reviewing and Edit-  
603 ing; **Alex Jonko:** Conceptualization, Supervision, Methodology, Investigation, Validation, Su-  
604 pervision, Reviewing and Editing, Project administration; **William Lassman:** Investigation,  
605 Reviewing and Editing; **Jeff Mirocha:** Software, Reviewing and Editing; **Branko Kosović:**  
606 Investigation, Reviewing and Editing; **Tirtha Banerjee:** Conceptualization, Supervision, Re-  
607 viewing and Editing, Project administration, Funding acquisition.

## 608 **Conflicts of Interest**

609 The authors declare no conflict of interest.

## 610 **Open Research**

611 The simulations used in this study are performed using the latest release of the WRF (v4.1.3)  
612 model (<https://github.com/wrf-model/WRF>).

## 613 **References**

614 J. Ching, R. Rotunno, M. LeMone, A. Martilli, B. Kosovic, P. Jimenez, and J. Dudhia. Con-  
615 vectively induced secondary circulations in fine-grid mesoscale numerical weather prediction  
616 models. *Monthly Weather Review*, 142(9):3284–3302, 2014.

617 A. Connolly, L. van Veen, J. Neher, B. J. Geurts, J. Mirocha, and F. K. Chow. Efficacy of the cell  
618 perturbation method in large-eddy simulations of boundary layer flow over complex terrain.  
619 *Atmosphere*, 12(1):55, 2021.

620 J. W. Deardorff. Numerical investigation of neutral and unstable planetary boundary layers.  
621 *Journal of Atmospheric Sciences*, 29(1):91–115, 1972.

622 J. W. Deardorff. Stratocumulus-capped mixed layers derived from a three-dimensional model.  
623 *Boundary-layer meteorology*, 18:495–527, 1980.

624 L. Di Mare, M. Klein, W. Jones, and J. Janicka. Synthetic turbulence inflow conditions for  
625 large-eddy simulation. *Physics of Fluids*, 18(2):025107, 2006.

626 P. Giani, M. G. Genton, and P. Crippa. Modeling the convective boundary layer in the terra  
627 incognita: Evaluation of different strategies with real-case simulations. *Monthly Weather*  
628 *Review*, 150(5):981–1001, 2022.

629 S. Haupt, L. K. Berg, A. Decastro, D. J. Gagne, P. Jimenez, T. Juliano, B. Kosovic, J. D. Mirocha,  
630 E. Quon, J. Sauer, et al. Report of the atmosphere to electrons mesoscale-to-microscale cou-  
631 pling project (fy2019). Technical report, Pacific Northwest National Lab.(PNNL), Richland,  
632 WA (United States . . . , 2019a.

633 S. E. Haupt, B. Kosovic, W. Shaw, L. K. Berg, M. Churchfield, J. Cline, C. Draxl, B. Ennis,  
634 E. Koo, R. Kotamarthi, et al. On bridging a modeling scale gap: Mesoscale to microscale  
635 coupling for wind energy. *Bulletin of the American Meteorological Society*, 100(12):2533–2550,  
636 2019b.

637 S. E. Haupt, R. Arthur, A. Decastro, D. J. Gagne, A. Jonko, B. Kosovic, T. Mccandless, R. K.  
638 Rai, L. K. Berg, S. Dettling, et al. Fy 2020 report of the atmosphere to electrons land-  
639 based mesoscale-to-microscale coupling project. Technical report, Pacific Northwest National  
640 Lab.(PNNL), Richland, WA (United States), 2020.

641 S.-Y. Hong, Y. Noh, and J. Dudhia. A new vertical diffusion package with an explicit treatment  
642 of entrainment processes. *Monthly weather review*, 134(9):2318–2341, 2006.

643 M. Jähn, D. Muñoz-Esparza, F. Chouza, O. Reitebuch, O. Knoth, M. Haarig, and A. Ansmann.  
644 Investigations of boundary layer structure, cloud characteristics and vertical mixing of aerosols  
645 at barbados with large eddy simulations. *Atmospheric Chemistry and Physics*, 16(2):651–674,  
646 2016.

- 647 P. A. Jiménez, J. Dudhia, J. F. González-Rouco, J. Navarro, J. P. Montávez, and E. García-  
648 Bustamante. A revised scheme for the wrf surface layer formulation. *Monthly weather review*,  
649 140(3):898–918, 2012.
- 650 A. Keat, U. Piomelli, E. Ballaras, and H. Kaltenbach. A priori and a posteriori tests of inflow  
651 conditions for large-eddy simulations. *Phys. Fluids*, 16:4696–4712, 2004.
- 652 M. Klein, A. Sadiki, and J. Janicka. A digital filter based generation of inflow data for spatially  
653 developing direct numerical or large eddy simulations. *Journal of computational Physics*, 186  
654 (2):652–665, 2003.
- 655 B. Kosović. Subgrid-scale modelling for the large-eddy simulation of high-reynolds-number  
656 boundary layers. *Journal of Fluid Mechanics*, 336:151–182, 1997.
- 657 H. Le, P. Moin, and J. Kim. Direct numerical simulation of turbulent flow over a backward-facing  
658 step. *Journal of fluid mechanics*, 330:349–374, 1997.
- 659 Y. Liu, T. Warner, Y. Liu, C. Vincent, W. Wu, B. Mahoney, S. Swerdlin, K. Parks, and J. Boehn-  
660 ert. Simultaneous nested modeling from the synoptic scale to the les scale for wind energy  
661 applications. *Journal of Wind Engineering and Industrial Aerodynamics*, 99(4):308–319, 2011.
- 662 L. Mazzaro, E. Koo, D. Muñoz-Esparza, J. Lundquist, and R. Linn. Random force perturba-  
663 tions: A new extension of the cell perturbation method for turbulence generation in multiscale  
664 atmospheric boundary layer simulations. *Journal of Advances in Modeling Earth Systems*, 11  
665 (7):2311–2329, 2019.
- 666 L. J. Mazzaro, D. Muñoz-Esparza, J. K. Lundquist, and R. R. Linn. Nested mesoscale-to-  
667 les modeling of the atmospheric boundary layer in the presence of under-resolved convective  
668 structures. *Journal of Advances in Modeling Earth Systems*, 9(4):1795–1810, 2017.
- 669 J. Mirocha, J. Lundquist, and B. Kosović. Implementation of a nonlinear subfilter turbulence  
670 stress model for large-eddy simulation in the advanced research wrf model. *Monthly Weather*  
671 *Review*, 138(11):4212–4228, 2010.
- 672 J. Mirocha, B. Kosović, and G. Kirkil. Resolved turbulence characteristics in large-eddy simula-  
673 tions nested within mesoscale simulations using the weather research and forecasting model.  
674 *Monthly Weather Review*, 142(2):806–831, 2014.

- 675 C.-H. Moeng and P. P. Sullivan. A comparison of shear-and buoyancy-driven planetary boundary  
676 layer flows. *Journal of Atmospheric Sciences*, 51(7):999–1022, 1994.
- 677 C.-H. Moeng and J. C. Wyngaard. Statistics of conservative scalars in the convective boundary  
678 layer. *Journal of Atmospheric Sciences*, 41(21):3161–3169, 1984.
- 679 A. S. Monin and A. M. Obukhov. Basic laws of turbulent mixing in the surface layer of the  
680 atmosphere. *Contrib. Geophys. Inst. Acad. Sci. USSR*, 151(163):e187, 1954.
- 681 D. Muñoz-Esparza and B. Kosović. Generation of inflow turbulence in large-eddy simulations of  
682 nonneutral atmospheric boundary layers with the cell perturbation method. *Monthly Weather*  
683 *Review*, 146(6):1889–1909, 2018.
- 684 D. Muñoz-Esparza, B. Kosović, C. García-Sánchez, and J. Van Beeck. Nesting turbulence in an  
685 offshore convective boundary layer using large-eddy simulations. *Boundary-layer meteorology*,  
686 151:453–478, 2014a.
- 687 D. Muñoz-Esparza, B. Kosović, J. Mirocha, and J. van Beeck. Bridging the transition from  
688 mesoscale to microscale turbulence in numerical weather prediction models. *Boundary-layer*  
689 *meteorology*, 153(3):409–440, 2014b.
- 690 D. Muñoz-Esparza, B. Kosović, J. Van Beeck, and J. Mirocha. A stochastic perturbation method  
691 to generate inflow turbulence in large-eddy simulation models: Application to neutrally strat-  
692 ified atmospheric boundary layers. *Physics of Fluids*, 27(3):035102, 2015.
- 693 D. Muñoz-Esparza, J. A. Sauer, R. R. Linn, and B. Kosović. Limitations of one-dimensional  
694 mesoscale pbl parameterizations in reproducing mountain-wave flows. *Journal of the Atmo-*  
695 *spheric Sciences*, 73(7):2603–2614, 2016.
- 696 D. Muñoz-Esparza, J. K. Lundquist, J. A. Sauer, B. Kosović, and R. R. Linn. Coupled mesoscale-  
697 les modeling of a diurnal cycle during the cwex-13 field campaign: From weather to boundary-  
698 layer eddies. *Journal of Advances in Modeling Earth Systems*, 9(3):1572–1594, 2017.
- 699 M. Pamiès, P.-E. Weiss, E. Garnier, S. Deck, and P. Sagaut. Generation of synthetic turbulent  
700 inflow data for large eddy simulation of spatially evolving wall-bounded flows. *Physics of fluids*,  
701 21(4):045103, 2009.

- 702 R. K. Rai, L. K. Berg, B. Kosović, J. D. Mirocha, M. S. Pekour, and W. J. Shaw. Comparison of  
703 measured and numerically simulated turbulence statistics in a convective boundary layer over  
704 complex terrain. *Boundary-Layer Meteorology*, 163:69–89, 2017a.
- 705 R. K. Rai, L. K. Berg, M. Pekour, W. J. Shaw, B. Kosovic, J. D. Mirocha, and B. L. Ennis.  
706 Spatiotemporal variability of turbulence kinetic energy budgets in the convective boundary  
707 layer over both simple and complex terrain. *Journal of Applied Meteorology and Climatology*,  
708 56(12):3285–3302, 2017b.
- 709 J. A. Sauer, D. Muñoz-Esparza, J. M. Canfield, K. R. Costigan, R. R. Linn, and Y.-J. Kim. A  
710 large-eddy simulation study of atmospheric boundary layer influence on stratified flows over  
711 terrain. *Journal of the Atmospheric Sciences*, 73(7):2615–2632, 2016.
- 712 W. C. Skamarock, J. B. Klemp, J. Dudhia, D. O. Gill, Z. Liu, J. Berner, W. Wang, J. G. Powers,  
713 M. G. Duda, D. M. Barker, et al. A description of the advanced research wrf model version 4.  
714 *National Center for Atmospheric Research: Boulder, CO, USA*, 145:145, 2019.
- 715 C. M. Smith and E. D. Skyllingstad. Investigation of upstream boundary layer influence on  
716 mountain wave breaking and lee wave rotors using a large-eddy simulation. *Journal of the*  
717 *Atmospheric Sciences*, 66(10):3147–3164, 2009.
- 718 A. Spille-Kohoff and H.-J. Kaltenbach. Generation of turbulent inflow data with a pre-  
719 scribed shear-stress profile. Technical report, TECHNISCHE UNIV BERLIN (GERMANY)  
720 HERMANN-FOTTINGER INST FUR STROMUNGSMECHANIK, 2001.
- 721 R. B. Stull. *An introduction to boundary layer meteorology*, volume 13. Springer Science &  
722 Business Media, 1988.
- 723 G. R. Tabor and M. Baba-Ahmadi. Inlet conditions for large eddy simulation: A review. *Com-  
724 puters & Fluids*, 39(4):553–567, 2010.
- 725 C. Talbot, E. Bou-Zeid, and J. Smith. Nested mesoscale large-eddy simulations with wrf: Per-  
726 formance in real test cases. *Journal of Hydrometeorology*, 13(5):1421–1441, 2012.
- 727 Z.-T. Xie and I. P. Castro. Efficient generation of inflow conditions for large eddy simulation of  
728 street-scale flows. *Flow, turbulence and combustion*, 81(3):449–470, 2008.

- 729 F. J. Zajaczkowski, S. E. Haupt, and K. J. Schmehl. A preliminary study of assimilating numerical  
730 weather prediction data into computational fluid dynamics models for wind prediction. *Journal*  
731 *of Wind Engineering and Industrial Aerodynamics*, 99(4):320–329, 2011.
- 732 J. Zhong, X. Cai, and Z.-T. Xie. Implementation of a synthetic inflow turbulence generator in  
733 idealised wrf v3. 6.1 large eddy simulations under neutral atmospheric conditions. *Geoscientific*  
734 *Model Development*, 14(1):323–336, 2021.
- 735 B. Zhou and F. K. Chow. Nighttime turbulent events in a steep valley: A nested large-eddy  
736 simulation study. *Journal of the Atmospheric Sciences*, 70(10):3262–3276, 2013.